Sensitivity of Mild Hydrothermal Synthesis to the Reaction Conditions: Targeting Mixed-Metal Hexagonal Tungsten Bronze Fluorides $A_xM^{2+}{}_xM^{3+}{}_{(1-x)}F_3$ to Investigate their Magnetic Behavior

Lakshani W. Masachchi, Navindra Keerthisinghe, Anna A. Berseneva, Gregory Morrison, Mark D. Smith, Logan S. Breton, Juliano Schorne-Pinto, Mina Aziziha and Hans-Conrad zur Loye*

Department of Chemistry and Biochemistry, University of South Carolina, Columbia, SC, 29208, United States

*Corresponding author. E-mail: zurloye@mailbox.sc.edu

Abstract

The synthesis of five quaternary hexagonal tungsten bronze (HTB) fluorides $A_xM^{2+}{}_xM^{3+}{}_{(1-x)}F_3$, ($A$ = Cs and Rb; M^{2+} = Co^{2+}, Ni^{2+} and Zn^{2+}; and M^{3+} = V^{3+}) *via* a mild hydrothermal route is reported. The crystal structures and compositions were determined using a combination of single-crystal X-ray diffraction, Rietveld refinement of powder X-ray diffraction data, and inductively coupled plasma optical emission spectroscopy analysis. This study highlights the sensitivity of the mild hydrothermal method on the reaction temperature, solvent system, and quantity of starting reagents that directly influence the selective synthesis of kinetically stabilized fluoride materials, including hydrated fluorides, β-pyrochlores and HTB. The magnetic susceptibility and isothermal magnetization data for all five compounds were collected, which revealed the existence of a strong antiferromagnetic component in these phases. The presence of the Kagome layer in the structure results in geometrical frustration and leads to frustration indexes ranging from 7 to 13 for these compounds.

Introduction

In recent years, the concept of magnetic frustration has garnered significant attention, as such systems can exhibit a range of exotic and degenerate magnetic ground states, such as spin glass, spin ice, and spin liquid states.[1] The simple definition of magnetic frustration is the inability of spins to achieve an ordered arrangement to minimize the total energy of the system. When such frustration occurs due to the geometry of the crystal structure of the material, it is referred to as geometric frustration. Geometric magnetic frustration arises, in particular, in crystal structures that feature a triangular arrangement of the magnetic cations that engage in antiferromagnetic interactions that cannot all be satisfied simultaneously.[2–4] We distinguish between 2D and 3D lattices with frustrated magnetism by considering the topology of the structures that exhibit corner and edge-sharing triangular lattices and corner and edge-sharing tetrahedral lattices, respectively. Many existing materials fall into one of two groups, either the 2D corner-sharing triangular lattices, such as the Kagome layer type structures (e.g., hexagonal tungsten bronze structure) or the 3D corner-sharing tetrahedral networks (e.g., pyrochlore).[2,5,6] Fluorides crystallizing in these structure types have been extensively investigated in recent years because of their interesting magnetic interactions at accessible temperatures and because they can accommodate many low oxidation state transition metals that, for charge balance reasons, cannot be accommodated into analogous oxide structures.[7–9]

Both hexagonal tungsten bronze and β-pyrochlore materials can compositionally be grouped with the perovskite family of structures, having the general composition of A_xMF_3 (x varies from 0 to 1), where the *A* site is occupied by a large monovalent cation such as K, Rb, and Cs, while M is a transition metal exhibiting two different oxidation states (M^{3+}/M^{2+}).[10,11,12] The A_xMF_3 framework consists of a three-dimensional corner-sharing octahedral (MF_6) framework. If we consider the case where x = 0, or a MF_3 composition, it can correspond to the rhombohedral FeF_3 or to the cubic ReO_3 structure where, in the latter case, a cuboctahedral vacancy exists in the middle of the cell. Conversely, if the cuboctahedral vacancy is fully occupied by an *A* cation, x = 1, then the cubic AMF_3 perovskite structure is obtained.[11] Interestingly, partial occupancy of the *A* cations inside the structure gives rise to a variety of different structure types whose existence depends on both the degree of the *A*-site occupancy and the size of the *A* cation (Figure 1). Fluoride phases of the type A_xMF_3 (*A* = K, Rb or Cs and M = V, Cr, Fe), with partial occupancies of the *A*

cation, were reported several years ago[13,14]. In each system the hexagonal tungsten bronze (HTB) structure spans the composition x ≈ 0.18–0.33, and the β-pyrochlore structure forms for *A* = Rb or Cs at x ≈ 0.40–0.60. The tetragonal tungsten bronze (TTB) structure exists for K_xMF_3 (x ≈ 0.40–0.60). Typically, larger cations (*A* = Rb and Cs) favor the β-pyrochlore structure over the TTB structure.[13–17]

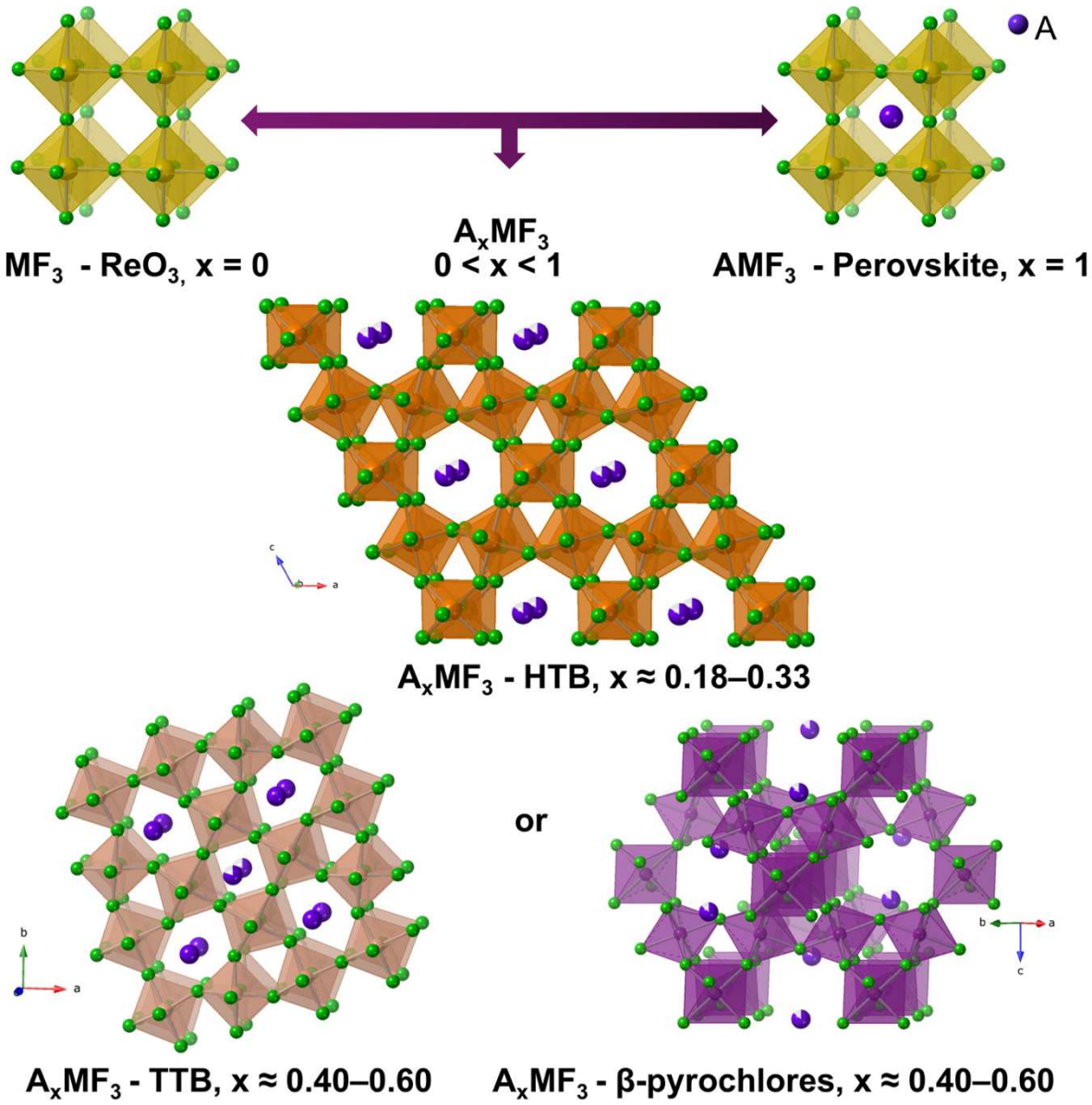

Figure 1. Illustration of the *A*-site occupancy range in A_xMF_3 for the different structure types.

Depending on the *A*-site occupancy and the size of the *A*-site cation, the octahedral building block connectivity changes, which results in different topologies for A_xMF_3 compounds. The MF_6 octahedra in both the β-pyrochlore and the HTB structures are arranged to form six-membered rings that are part of one layer (Kagome layer). In the HTB structure, these Kagome layers are stacked parallel to each other, resulting in one-dimensional tunnels. In the β-pyrochlore structure, three different Kagome layers are interconnected along different directions, forming three-dimensional tunnels (Figure 2). Many β-pyrochlore fluorides were reported in cubic and orthorhombic symmetries and their magnetic behavior was extensively investigated.[18,19] In our recent paper, we discussed the synthesis, structure, and magnetic properties of seven new mixed-metal β-pyrochlores, $Cs_{0.86}Co_{0.86}V_{1.14}F_6$, $Cs_{0.9}Ni_{0.9}V_{1.1}F_6$, $Cs_{0.9}Zn_{0.9}V_{1.1}F_6$, $CsZnFeF_6$, $Rb_{0.93}Co_{0.93}V_{1.07}$. In contrast to the β-pyrochlore fluorides, no mixed-transition-metal HTB fluorides have been reported previously; only A_xFeF_3, A_xCrF_3, and A_xVF_3 (*A* = Na, K, Rb, and Cs) have been reported to crystallize in the HTB structure.[14–17] The reported HTB compositions were prepared via solid-state reactions and mild hydrothermal synthesis routes.[14–17]

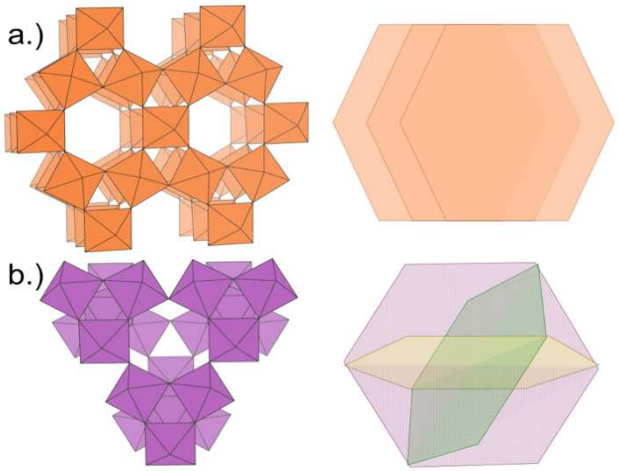

Figure 2. (a.) Illustration of the one-dimensional hexagonal tunnel connectivity of the HTB structure (left) and parallel Kagome layers (right). (b.) Illustration of the three-dimensional hexagonal tunnel connectivity in the β-pyrochlore structure (left) and interconnected Kagome layers (right).

The mild hydrothermal method is one of the most promising methods for targeting new materials crystallizing in various structure types.[20–23] Apart from thermodynamic phases, mild hydrothermal conditions often yield kinetically stabilized products due to the low reaction

temperatures and fast solution kinetics. Hydrothermal (solvothermal) synthesis is typically carried out in a closed system at a temperature above the boiling point of the solvent and operates at autogenous pressure, which facilitates the dissolution of reagents and also promotes the growth of single crystals.[24] Solution-based synthesis is influenced by various factors, including the physicochemical properties of the precursors, such as solubility and thermal stability; the characteristics of the solvent used, such as solvation strength, polarity, and viscosity; and the thermodynamic conditions employed, including pressure and temperature.[25,26] Previous reports in the literature discussed the synthesis of oxide based β-pyrochlores and HTB structures by adjustment of the mild hydrothermal reaction conditions, including the pH of the reaction mixture.[19] However, a comprehensive investigation of the sensitivity of the mild hydrothermal method for obtaining different fluoride compositions and structures in the same compositional phase space by varying the reaction conditions has not been conducted.

Herein, we report the mild hydrothermal synthesis of five hexagonal tungsten bronze-type mixed-metal fluorides, $Cs_{0.29}Co_{0.29}V_{0.71}F_3$, $Cs_{0.28}Ni_{0.28}V_{0.72}F_3$, $Cs_{0.27}Zn_{0.27}V_{0.73}F_3$ $Rb_{0.28}Co_{0.28}V_{0.72}F_3$ and $Rb_{0.28}Ni_{0.28}V_{0.72}F_3$, that crystallize in monoclinic symmetry. Their syntheses, crystal structures, and magnetic properties are discussed. For the first time, a detailed examination of how the mild hydrothermal reaction conditions, including reaction temperature, solvent volume, and reagent concentration, direct the formation of the different fluoride structures is presented. These insights will aid in tailoring the mild hydrothermal synthesis to target new fluoride complexes with desired compositions. In addition, we have studied the thermal behavior of each compound via simultaneous thermogravimetric and differential thermal analysis (TGA/DTA) and describe the observed HTB to cubic β-pyrochlore phase transition that occurs at elevated temperatures.

Experimental

Synthesis

Materials: RbCl (99.8%, Alfa Aesar), CsCl (99%, Alfa Aesar), V_2O_3 (95%, Alfa Aesar), $Ni(CH_3COO)_2•4H_2O$ (98%, Sigma-Aldrich), $Zn(CH_3COO)_2•2H_2O$ (98%, Fisher), $Co(CH_3COO)_2•4H_2O$ (98%, Alfa Aesar), $Zn(C_5H_7O_2)_2•2H_2O$ (98%, Strem) and HF (49% aqueous, VWR®) were used as received.

Caution! Hydrofluoric acid is highly corrosive and acutely toxic and must be handled with proper safety precautions in a well-ventilated space. In case of exposure, proper treatment with immediate medical attention is essential.

Using the mild hydrothermal synthesis,[21,27] five mixed-metal hexagonal tungsten bronze type fluorides with compositions $A_xM^{2+}{}_xM^{3+}{}_{(1-x)}F_3$ (*A*= Cs and Rb; M^{2+} = Ni, Co, and Zn; M^{3+} = V) were successfully synthesized. The starting materials (Table 1) were added to a 23 mL PTFE liner along with 3 or 6 mL of 49% aqueous HF and sealed in a steel autoclave. The autoclave was heated to 200 °C at 10 °C/min in a programmable convection oven, allowed to dwell for 12 hours, and cooled to room temperature by shutting off the oven. The polycrystalline powders were isolated *via* vacuum filtration and washed with water and acetone. Reactions were also carried out by changing the reagent ratio, temperature profile, and HF volume to observe their impact on the formation of other products (Tables S1 and S2).

Table 1. Starting Reagents for HTB synthesis.

	Chemical Formula	$M(CH_3COO)_2 \cdot 4H_2O$/ $Zn(C_5H_7O_2)_2 \cdot 2H_2O$ (mmol)	V_2O_3 (mmol)	*A*Cl (mmol)	49% HF (mL)
1	$Cs_{0.29}Co_{0.29}V_{0.71}F_3$	2	1	2	3
2	$Cs_{0.28}Ni_{0.28}V_{0.72}F_3$	2	1	2	3
3	$Cs_{0.27}Zn_{0.27}V_{0.73}F_3$	2	1	2	6
4	$Rb_{0.28}Co_{0.28}V_{0.72}F_3$	4	1	2	3
5	$Rb_{0.28}Ni_{0.28}V_{0.72}F_3$	4	1	2	3

Single-Crystal X-ray Diffraction (SXRD)

Single-crystal X-ray diffraction data were collected at 298(2) or 301(2) K using a Bruker D8 QUEST diffractometer equipped with a PHOTON-II area detector and an Incoatec microfocus source (Mo K_α radiation, λ = 0.71073 Å). The crystals were mounted on a microloop using immersion oil. The raw area detector data frames were reduced and corrected for absorption effects using the SAINT+ and SADABS programs.[28,29] Final unit cell parameters were determined by least-squares refinement. Initial structural models were obtained with SHELXT.[30] Subsequent difference Fourier calculations and full-matrix least-squares refinements against F^2 were performed with SHELXL-2018 using Olex2.[31]

The structures possess obvious hexagonal pseudosymmetry, as shown by the reported monoclinic lattice parameters ($a = c$, $\beta \approx 120.0°$). However, no physically reasonable solution could be obtained in any hexagonal space group. Subsequently, the diffraction pattern was indexed, data were integrated, and solutions were attempted in triclinic, monoclinic, and orthorhombic crystal systems. The best structural model of several attempted is as a pseudomerohedrical twin in the monoclinic system. The TwinRotMat functionality in the Platon suite was used to determine the relevant twin law, [0 0 -1 / 0 -1 0 / -1 0 0] for $Cs_{0.29}Co_{0.29}V_{0.71}F_3$ and $Cs_{0.28}Ni_{0.28}V_{0.72}F_3$ and [-1 0 0 / 0 -1 0 / 1 0 1] for $Cs_{0.27}Zn_{0.27}V_{0.73}F_3$, which was then accounted for using the TWIN and BASF commands in ShelXL.[32] The major twin domain volume fraction refined to 0.507 for the $Cs_{0.29}Co_{0.29}V_{0.71}F_3$, 0.512 for $Cs_{0.28}Ni_{0.28}V_{0.72}F_3$ and 0.451 for $Cs_{0.27}Zn_{0.27}V_{0.73}F_3$. The site occupancy factor (*sof*) for cesium refined to significantly less than full occupancy. This was accompanied by a substantial decrease in the *R*-values as well as by normalization of the anisotropic displacement parameters of most of the fluorine atoms from 'non-positive definite' to sensible values. The *sof* values of the three unique transition metal sites each refined to greater than full occupancy by vanadium or to less than full occupancy by cobalt, nickel or zinc. This was interpreted as M^{2+}/V^{3+} mixing on each site. The presence of both M and V in the crystal was corroborated by elemental analysis (EDS). For preliminary models, the total *sof* of each transition metal site was constrained to sum to one, resulting in a compositions within 0.10 e- of electroneutrality. Such a small deviation is negligible, as further constraining the composition to electroneutrality resulted in no change to the *R*-values or difference map features. It is likely that the relative similarity of M and V atomic scattering factors causes less accurate atomic ratios

on each site. Alternatively, transition metal site vacancies may exist. For the final model, the transition metal site fractional occupancies were constrained to satisfy charge balance. More details about the structure solution of $Cs_{0.28}Ni_{0.28}V_{0.72}F_3$ are included in the supporting information (S.I.) as representative of mixed- metal structures. For $Cs_{0.27}Zn_{0.27}V_{0.73}F_3$, refinement in $P2_1/m$ resulted in high R-values and large fluorine ADPs even after accounting for twinning. For this reason, the structure was refined in the lower symmetry space group $P2_1$ which resulted in much better refinement statistics and atomic parameters. The crystallographic data and results of the diffraction experiments are summarized in Table 2.

Table 2. Crystallographic data for **1**-**3**.

	(1) $Cs_{0.29}Co_{0.29}V_{0.71}F_3$	**(2)** $Cs_{0.28}Ni_{0.28}V_{0.72}F_3$	**(3)** $Cs_{0.27}Zn_{0.27}V_{0.73}F_3$
Formula weight	149.29	147.42	148.19
Temperature, K	298(2)	301(2)	298(2)
Crystal system	monoclinic	monoclinic	monoclinic
Space group, Z	$P2_1/m$	$P2_1/m$	$P2_1$
a, Å	7.4534(7)	7.4214(7)	7.4198(10)
b, Å	7.6383(7)	7.5938(7)	7.5904(10)
c, Å	7.4492(7)	7.4230(7)	7.4194(10)
α, *deg*	90		
β, deg	120.024(3)	120.024(3)	119.9980(10)
γ, *deg*	90		
Volume, $Å^3$	367.19(6)	362.20(6)	361.880(9)
ρ_{calc}, g/cm^3	4.051	4.005	4.080
μ/mm^{-1}	9.143	9.177	9.622
F(000)	404.0	401.0	402.0
Crystal size, mm^3	0.016 × 0.012 × 0.003	0.060 × 0.020 × 0.010	0.040 × 0.030 × 0.007
Radiation (λ, Å)	0.71073		
2θ range, deg.	5.334 – 59.98	5.364 – 65.168	5.366 – 72.646
Reflections collected	27649	17383	45198
Data/restraints/parameters	1131/0/75	1409/1/76	3518/2/119
Goodness-of-fit	1.219	1.223	1.081
R_1 [I>=2σ (I)]	0.0209	0.0292	0.0316
wR_2 [all data]	0.0520	0.0540	0.0772
Largest diff. peak/hole, e $Å^{-3}$	1.24/–0.57	1.18/–0.63	1.90/–1.16
R_{int}, %	3.52	3.56	3.49

Powder X-ray Diffraction (PXRD)

Powder X-ray diffraction data for $Cs_{0.29}Co_{0.29}V_{0.71}F_3$, $Cs_{0.28}Ni_{0.28}V_{0.72}F_3$, and $Cs_{0.27}Zn_{0.27}V_{0.73}F_3$ were collected on a Bruker D2 Phaser powder X-ray diffractometer using Cu K_α radiation to confirm the phase purity of polycrystalline samples obtained by grinding single crystals (Figures S1−S3). The data were collected over the angular range of 5−65° 2θ using a step size of 0.04° and a scan rate of 1°/min.

PXRD data of $Rb_{0.28}Co_{0.28}V_{0.72}F_3$ and $Rb_{0.28}Ni_{0.28}V_{0.72}F_3$ were collected on a Rigaku Ultima IV diffractometer equipped with a Cu K_α X-ray source and a DteX Ultra detector for the Rietveld refinement. The diffraction patterns were analyzed, fitted, and refined with the Rietveld/d-I pattern method using the TOPAS commercial v5 software for structure determination.

Rietveld Refinement

Rietveld refinements were performed operating TOPAS commercial v5 in launch mode using jEdit with macros for TOPAS (Figure 3).[33] The default approach was refining the unit cell parameters, the Gaussian and Lorentzian isotropic size parameters, scale factors, and Chebychev background parameters. The site occupancies and the temperature factors were fixed according to the isostructural $Cs_{0.28}Ni_{0.28}V_{0.72}F_3$ composition solved by SXRD. The atomic positions, except for F1, F2, F3, and F4, were fixed. In $Rb_{0.28}Co_{0.28}V_{0.72}F_3$, the F1, F2, F3, and F4 atom positions were refined under the restrained bond distances of Co1−F1, Co2−F2, Co1−F3, and V1−F4 bonds. The same atomic positions in $Rb_{0.28}Ni_{0.28}V_{0.72}F_3$ were refined under the restrained bond distances of Ni1−F1, Ni2−F2, V1−F3, and V1−F4 bonds. The preferred orientation (2, 0, −2) was used for $Rb_{0.28}Co_{0.28}V_{0.72}F_3$. A high-order spherical harmonic intensity correction for $Rb_{0.28}Ni_{0.28}V_{0.72}F_3$ was needed to refine the peak shapes further. Crystallographic information for the Rietveld refined structures is provided in Tables 3, S3, and S4.

Table 3. Crystallographic data for Rietveld structure refinements of **4** and **5**.

	(4) $\mathbf{Rb_{0.28}Co_{0.28}V_{0.72}F_3}$	**(5)** $\mathbf{Rb_{0.28}Ni_{0.28}V_{0.72}F_3}$
Crystal system	monoclinic	monoclinic
Space group, Z	$P2_1/m$	$P2_1/m$
a, Å	7.3911(3)	7.3863(4)
b, Å	7.5380(1)	7.4980(1)
c, Å	7.3823(3)	7.3584(3)
β, deg	119.838(2)	120.010(3)
R_{wp} (%)	1.07	3.19
R_p (%)	0.71	1.84
GOF	2.67	6.77

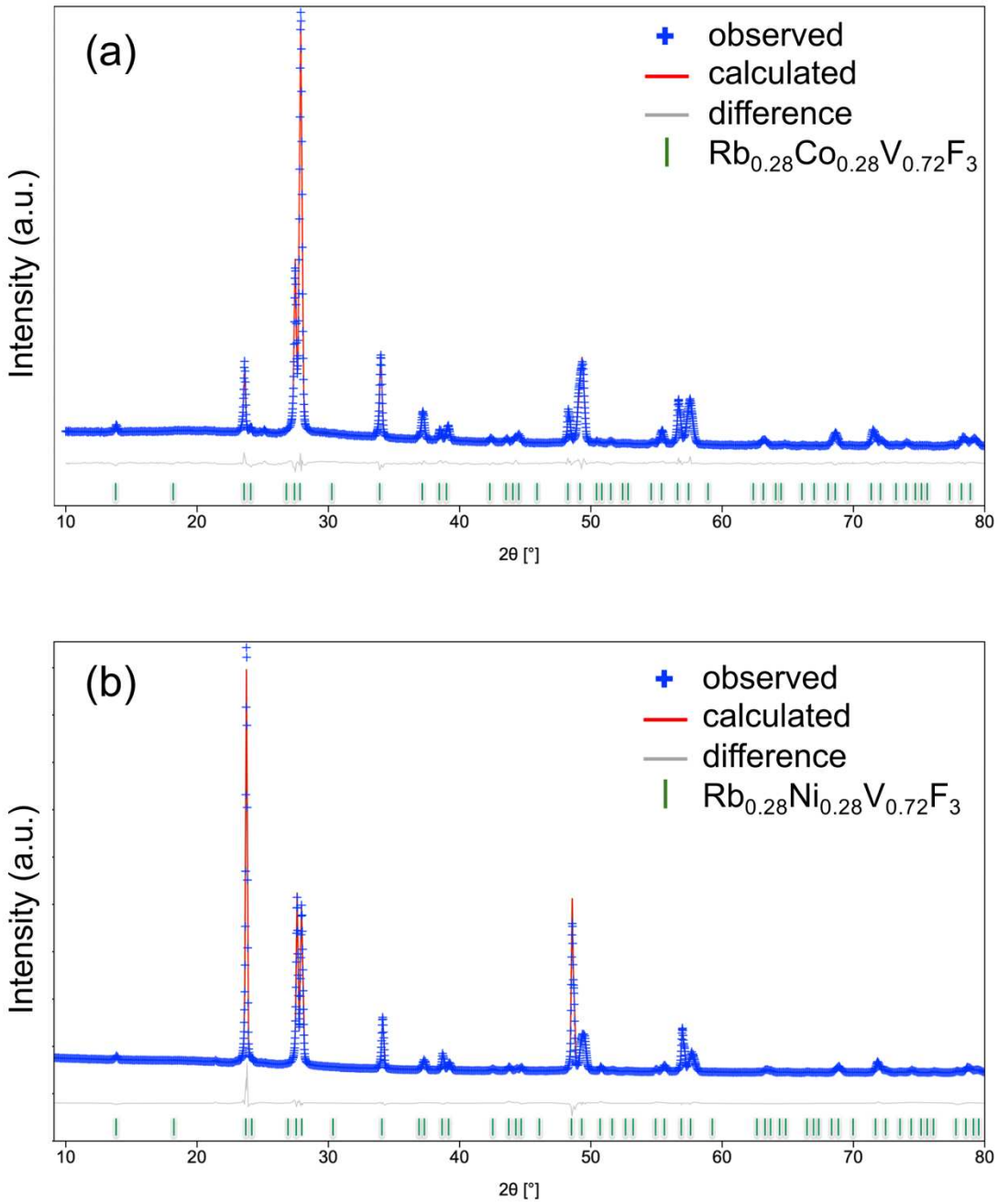

Figure 3. Rietveld refinement plots of $Rb_{0.28}Co_{0.28}V_{0.72}F_3$ (a) and $Rb_{0.28}Ni_{0.28}V_{0.72}F_3$ (b); red line is the Rietveld fit, blue +'s are the observed PXRD data, grey line is the residual, and the vertical green tick marks indicate the allowed Bragg reflections.

Energy-Dispersive Spectroscopy (EDS)

EDS was performed on single crystals using a TESCAN Vega-3 SBU scanning electron microscope (SEM) with a Thermo EDS attachment operated in low-vacuum mode (Table S5). The

crystals were mounted on an SEM stub with carbon tape and analyzed using 20 kV accelerating voltage and an accumulation time of 20 seconds.

Inductively coupled plasma optical emission spectroscopy (ICP-OES)

The molar ratio of $Rb_{0.28}Co_{0.28}V_{0.72}F_3$ and $Rb_{0.28}Ni_{0.28}V_{0.72}F_3$ samples were confirmed by ICP-OES (PerkinElmer Avio 200 spectrometer) on digested samples. Cs-containing samples were not measured in the ICP-OES due to its low ionization potential, resulting in a low sensitivity in the concentration range used in this work. Crystalline samples (≈ 2.0 mg) were loaded into a Teflon liner with 8 mL of aqua regia (HNO_3, HCl, and deionized water were mixed in a 4:8:3 volume ratio). The microwave digestion reaction was performed in PerkinElmer's Titan MPS 16 Position vessels digestion system using a Teflon liner. The digestion system was ramped to 175 °C and 30 bars in 30 min. The sample was held at that temperature and pressure for 10 minutes and cooled down to 50 °C in 125 min. Once at room temperature, the digested sample was diluted to the appropriate concentrations using a blank solution of 6.5 M HNO_3 (High-Purity Standards (HPS) Company). Calibrations for Co, Ni, Rb, and V used five to seven different concentrations and a blank between 0 to 10 ppm range (Table S6). All volumes were measured using a high precision pipettor (VWR Signature, listed accuracy ±1.6–0.6% and precision ≤0.4–0.15%).

Thermogravimetric Analysis

Thermogravimetric and differential thermal analysis (TGA/DTA) measurements were performed on polycrystalline powder samples using a TA Instruments SDT Q600 Thermogravimetric Analyzer and a platinum pan as the sample holder. Samples were heated from room temperature to the target temperature (600°C) at 10°C/min under a flow of nitrogen gas (100 mL/min), and the resulting powders were analyzed by PXRD for phase identification post-heating.

Magnetic Measurements

Susceptibility and magnetization measurements were performed on ground single crystals using a Quantum Design MPMS3 SQUID magnetometer. Susceptibility measurements were collected under zero-field cooled (ZFC) and field-cooled (FC) conditions in the temperature range of 2−300 K at an applied field of 0.1 T. Magnetization as a function of magnetic field was measured

at 2 K in an applied field ranging from −5 to +5 T. The raw data were corrected for radial offset and shape effects.[34]

Results and Discussion

Synthesis

The mild hydrothermal synthesis method is very effective for preparing many fluoride materials, which motivated us to use this approach to target the synthesis of new mixed-metal fluoride compounds.[21,35–37] Single crystals, along with polycrystalline powders, of the hexagonal tungsten bronze fluorides $A_xM^{2+}{}_xM^{3+}{}_{(1-x)}F_3$ (A = Cs and Rb; M^{2+} = Co^{2+}, Ni^{2+}, and Zn^{2+}; and M^{3+} = V^{3+}) were successfully obtained hydrothermally using HF as a simultaneous solvent and fluorinating agent at the relatively low temperatures of 200−220 °C. The conditions were optimized after several trial syntheses to obtain phase-pure single-crystal and polycrystalline products.

In addition to the hexagonal tungsten bronze (HTB) fluorides, we also observed several additional fluoride materials, including hydrated fluorides and β-pyrochlore fluorides, when slight changes were made to the mild hydrothermal reaction conditions. For example, phase pure samples of hexagonal tungsten bronze $Cs_{0.28}Ni_{0.28}V_{0.72}F_3$ were obtained when using 3 ml of HF for the synthesis. However, as water is introduced to the reaction, replacing HF in 0.5 mL increments with equal volumes of water, keeping all other reaction parameters identical, the β-pyrochlore phases started to appear (Figure S4). Once the amount of water reached more than 50% of the solvent system, phase pure samples of the β-pyrochlore structure were obtained (Figure 4). Comparing the HTB ($A_xM^{2+}{}_xM^{3+}{}_{(1-x)}F_3$, where x = 0.18−0.33) and β-pyrochlore phases ($A_xM^{2+}{}_xM^{3+}{}_{(1-x)}F_3$, where x = 0.40−0.50), we observe higher Cs incorporation into the β-pyrochlore phases. Based on our observation, it appears that CsCl dissolves more favorably in the presence of additional water. It was also reported that higher pH, which facilitates Cs ion incorporation, results in Cs ion-rich compounds.[19] It can be inferred that the solvent system and pH of the solution significantly influence the choice of the prominent phase by controlling the A cation incorporation. Moreover, the final product of the Cs phases is also affected by the reaction temperature and the ratio of the starting reagents. It is notably evident that elevated temperature and the presence of larger quantities of CsCl in the reaction mixture favour the β-pyrochlore $CsNiVF_6$ phase over $Cs_{0.28}Ni_{0.28}V_{0.72}F_3$ (Figure 5a).

We observed that the reaction conditions that resulted in the formation of the Cs-containing HTB phases did not also generate the Rb-based HTB phases, but rather resulted in only the hydrate fluoride phases $NiV_2F_8(H_2O)_2$ and $NiVF_5(H_2O)_2$ (Figure 4). However, further increasing the

quantity of RbCl or increasing the reaction temperature from 200 °C to 220 °C and diluting the HF concentration by replacing 0.5 ml HF with water resulted in the formation of the desired Rb-containing HTB phases. Moreover, we found that different amounts of Rb incorporation led to different structure types, including the HTB, β-pyrochlore, and $Rb_2(VO)F_4$ phases, which appears to depend on the dissolution of the Rb starting material (Figure 5b). The data indicate that the incorporation of Rb ions into the products is enhanced by higher reaction temperatures, elevated water content, and higher initial Rb concentrations in the solution.

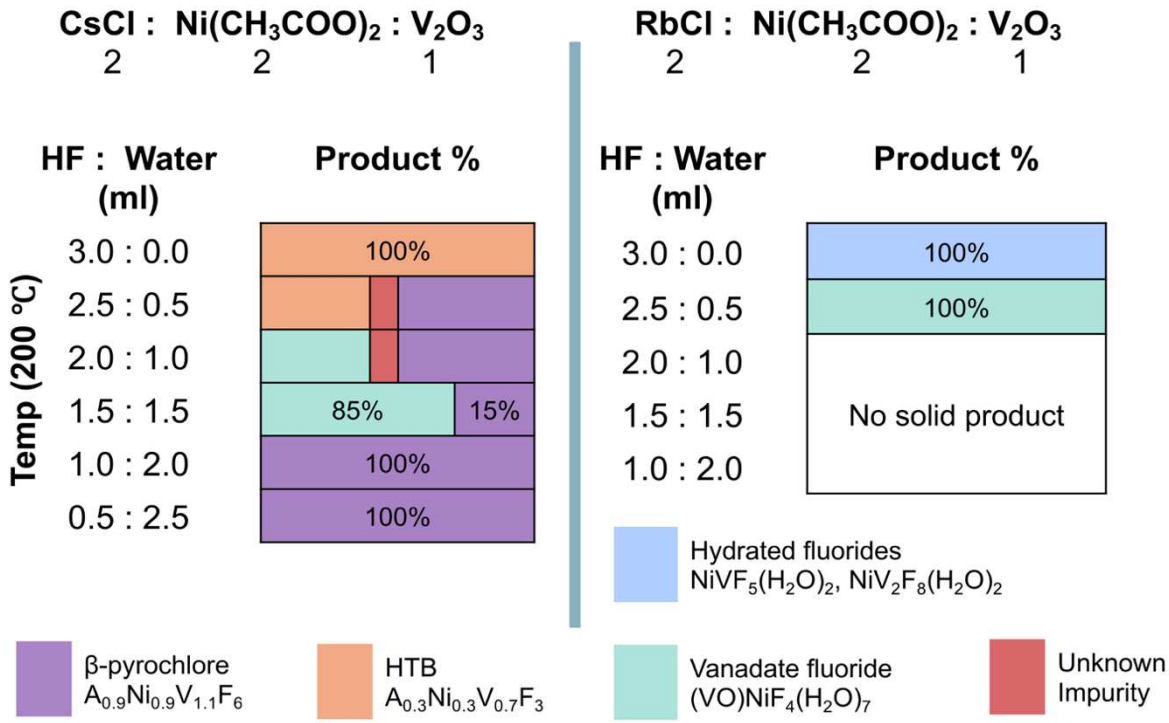

Figure 4. The reaction scheme detailing the formation of different products resulting from adjusting the HF to water ratio. Cs containing phases are listed on the left and Rb containing phases are listed on the right.

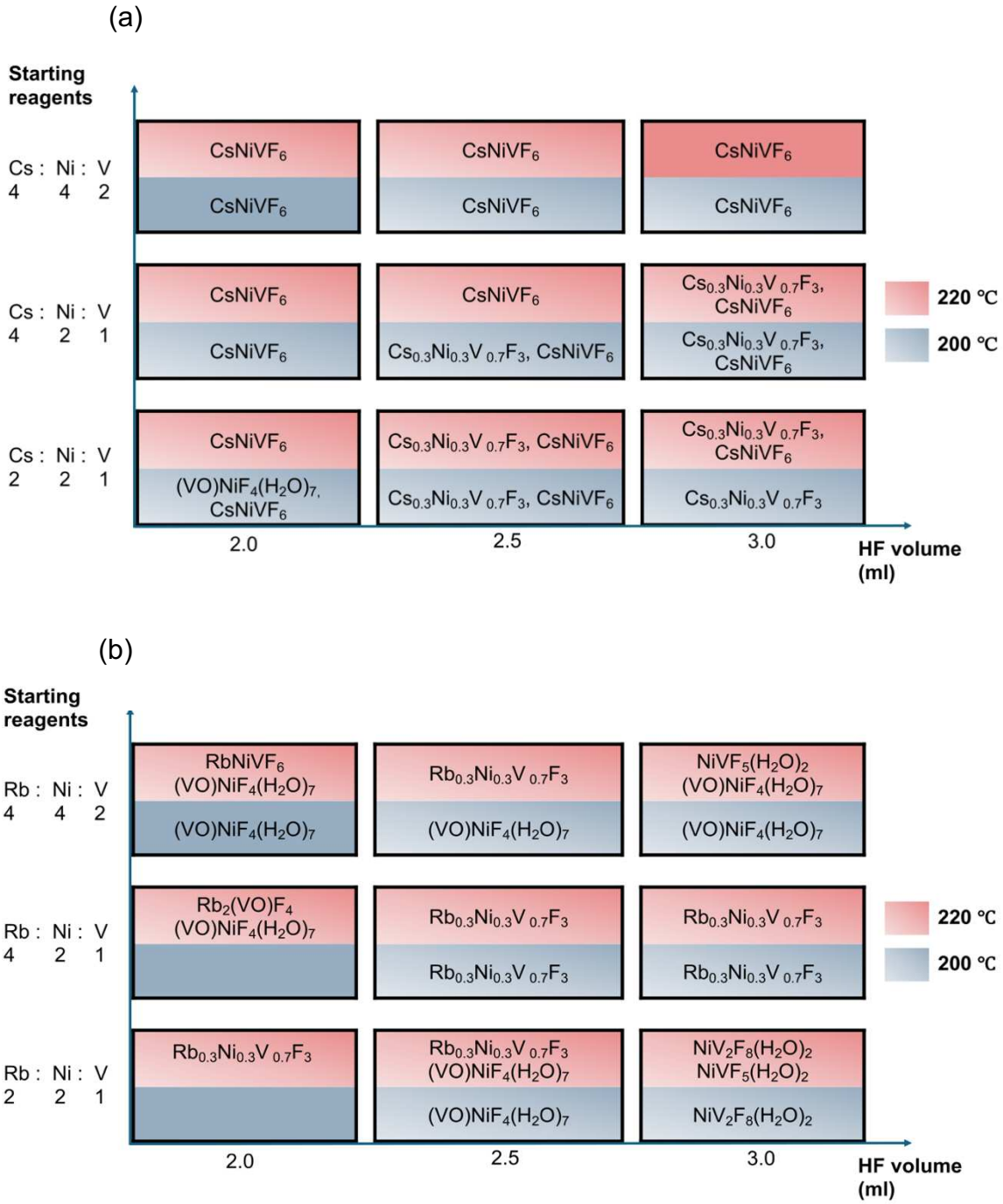

Figure 5. The reaction scheme detailing the formation of different products upon changing the HF volume, reagent ratio, and temperature. a) Cs phases; b) Rb phases.

In contrast to other phases, the $Cs_{0.27}Zn_{0.27}V_{0.73}F_3$ phase was obtained (Figure S3) when the starting reagent of Zn was changed from $Zn(CH_3COO)_2 \cdot 4H_2O$ to $Zn(C_5H_7O_2)_2 \cdot 2H_2O$ along with 6 ml of HF. Depending on the ratio of water to HF, either the β-pyrochlore, the HTB phase, or a mixture, is obtained (Figure 6). This study properly illustrates the sensitivity of the hydrothermal method

toward its reaction conditions and its potential to produce new fluoride materials by tailoring the mild hydrothermal synthesis.

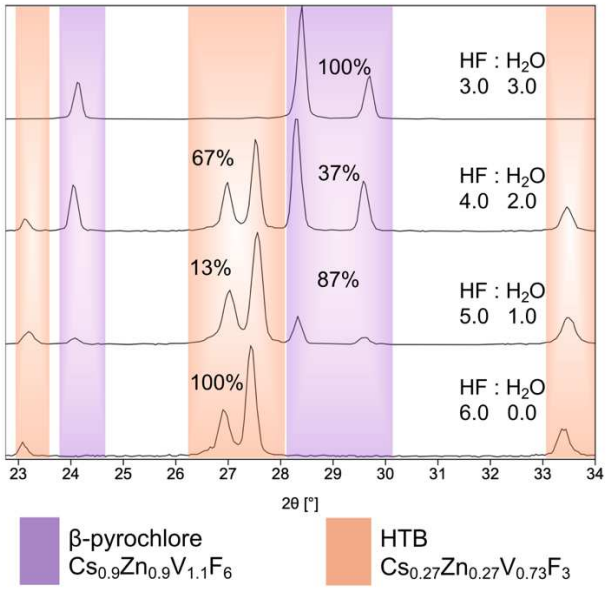

Figure 6. PXRD of the product for the reaction between $Zn(C_5H_7O_2)_2•2H_2O$, V_2O_3, and CsCl as a function of the HF volume.

Crystal Structure Description

Crystal structures of $Cs_{0.29}Co_{0.29}V_{0.71}F_3$, $Cs_{0.28}Ni_{0.28}V_{0.72}F_3$, and $Cs_{0.27}Zn_{0.27}V_{0.73}F_3$ were determined by SXRD. Structure solutions for $Rb_{0.28}Co_{0.28}V_{0.72}F_3$ and $Rb_{0.28}Ni_{0.28}V_{0.72}F_3$ were obtained by Rietveld refinement (Figure 3). Table 3 contains the refined parameters of Rp, Rwp, GOF, and lattice parameters. The low values of the reliability parameters (Rp, Rwp, and GOF, Table 3) demonstrate the excellent fit of the data and support that the $Rb_{0.28}Co_{0.28}V_{0.72}F_3$ and $Rb_{0.28}Ni_{0.28}V_{0.72}F_3$ compositions possess the same crystal structures as $Cs_{0.29}Co_{0.29}V_{0.71}F_3$ and $Cs_{0.28}Ni_{0.28}V_{0.72}F_3$, respectively.

The title compounds $Cs_{0.29}Co_{0.29}V_{0.71}F_3$, $Cs_{0.28}Ni_{0.28}V_{0.72}F_3$, $Rb_{0.28}Co_{0.28}V_{0.72}F_3$, and $Rb_{0.28}Ni_{0.28}V_3F_3$ crystallize in the monoclinic space group $P2_1/m$, while $Cs_{0.27}Zn_{0.27}V_{0.73}F_3$ crystallizes in the $P2_1$ space group. These compounds represent a new series of mixed-metal hexagonal tungsten bronze fluorides belonging to the $A_xM^{2+}{}_xM^{3+}{}_{(1-x)}F_3$ compositional family. The

three-dimensional framework of all compositions (**1-5**) primarily consists of $(M^{2+}/M^{3+})F_6$ corner-sharing octahedra that create triangular and hexagonal tunnels in the system. The *A* cations reside in the hexagonal tunnels, and the occupancy of the *A* cation site (*A* = Cs/Rb) is less than 1 in all the structures. The overall connectivity of the octahedra results in parallel Kagome layers in the *ac*-plane (Figure 7). Three unique M^{2+}/M^{3+} crystallographic sites, all of which exhibit anti-site mixing, create disorder in the structures. In this HTB family, for each site, the occupancy of V^{3+} is greater than that of M^{2+} (Figure 8).

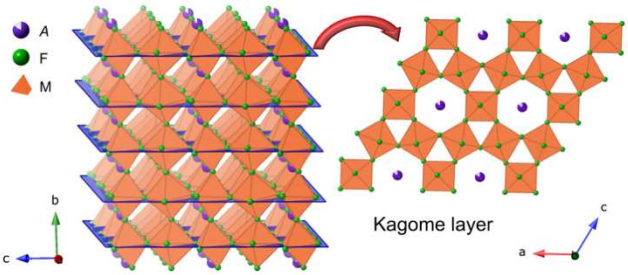

Figure 7. View of the monoclinic HTB crystal structure $A_xM^{2+}{}_xM^{3+}{}_{(1-x)}F_3$

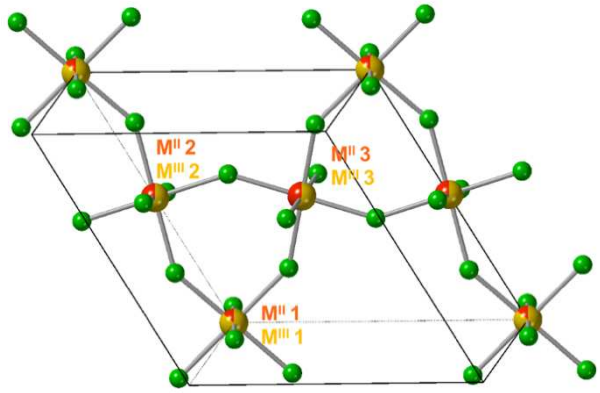

Figure 8. Schematic highlighting the fractional occupancies of the three independent transition metal sites.

Thermal Properties

The thermal properties of **1**−**5** were explored to study the structural stability of HTB upon heating (Figure S5). All the samples exhibited a 5−8% weight loss between 100−700 °C in the TGA plot, which can be attributed to the loss of surface water and decomposition of the materials. In the DTA plot, the first endothermic peak at 100 °C is related to the evaporation of the surface

water, and the peak at 550−675 °C corresponds to the structure transition (Figure S5). The transition to the cubic β-pyrochlore structure was confirmed by post-TGA PXRD. To confirm the nature of the transitions, $Cs_{0.29}Co_{0.29}V_{0.71}F_3$ samples were thermally quenched at 500 °C and 675 °C in a tube furnace under N_2 flow. PXRD of the sample quenched at 500 °C revealed the presence of both the HTB and the β-pyrochlore phases. On the other hand, the PXRD analysis of the sample quenched at 675 °C shows only the β-pyrochlore phase (Figure S6). This suggests that the mixed-metal HTB fluorides are less thermally stable than the β-pyrochlore ones. Upon further heating, beyond 700 °C, the material started to react with oxygen impurities in the SDT and decomposed to binary and ternary oxides.

Magnetic Properties

The HTB structure consists of parallel Kagome layers along the ac plane. Since the connectivity of the magnetic ions takes place within the Kagome layer, it results in geometrically frustrated magnetism.[37,38] To investigate the magnetic behavior of the title compounds, we collected zero field-cooled and field-cooled DC magnetic susceptibility vs. temperature and magnetization vs. field data, the results of which are summarized in Table 4.

Table 4. Magnetic Properties of **1**−**5**.

Chemical Formula	Magnetic Properties	Effective magnetic moment (μ_{eff}) (μ_B/F.U.)		θ_{CW} (K)	Magnetic ordering T (K)	Frustration Index
		observed	calculated			
$Cs_{0.29}Co_{0.29}V_{0.71}F_3$	antiferromagnetic	3.43	3.17	–45	6	7
$Cs_{0.28}Ni_{0.28}V_{0.72}F_3$	antiferromagnetic	2.38	2.83	–41	3	13
$Cs_{0.27}Zn_{0.27}V_{0.73}F_3$	antiferromagnetic	2.42	2.42	–42	4	11
$Rb_{0.28}Co_{0.28}V_{0.72}F_3$	antiferromagnetic	3.28	3.16	–47	6	7
$Rb_{0.28}Ni_{0.28}V_{0.72}F_3$	antiferromagnetic	2.50	2.83	–52	5	11

The magnetic susceptibility and inverse susceptibility as a function of temperature plots are shown in Figure 9. The high-temperature regions (150 to 300 K) of the plots were fit to the Curie-Weiss law $\chi = \frac{C}{T-\theta_{CW}}$, where χ is the magnetic susceptibility, C is the Curie constant, T is temperature, and θ_{CW} is the Weiss temperature.[21,37] C is related to the number of unpaired electrons and θ_{CW} is an approximate indicator of the magnetic coupling strength (superexchange interaction) between ions. Both cobalt-containing compounds ($Cs_{0.29}Co_{0.29}V_{0.71}F_3$ and $Rb_{0.28}Co_{0.28}V_{0.72}F_3$)

have an experimental magnetic moment that is larger than the spin-only moment, indicating the presence of spin-orbit coupling in Co^{2+}.[21,37]

These HTB compounds exhibit a magnetic transition at temperatures below 6 K while the large negative Weiss temperatures indicate the presence of strong antiferromagnetic interactions in these materials (Table 4).[39] The large negative Weiss temperatures, along with the low-temperature magnetic transition, yield a frustration index for these compounds between 7–13. Typically, the type and concentration of the magnetic ions impact the observed magnetic properties.[38] In this case, however, all five compositions show similar magnetic behavior despite having different M^{2+} ions. This highlights that adding M^{2+} cations, with or without unpaired electrons, appears to not significantly impact the magnetic behavior in this group of compositions. This may be due to the fact that only 30% of the M^{2+} cation is contained in the HTB structure, and that M^{3+} is the dominant contributor to the overall magnetic ion concentration.

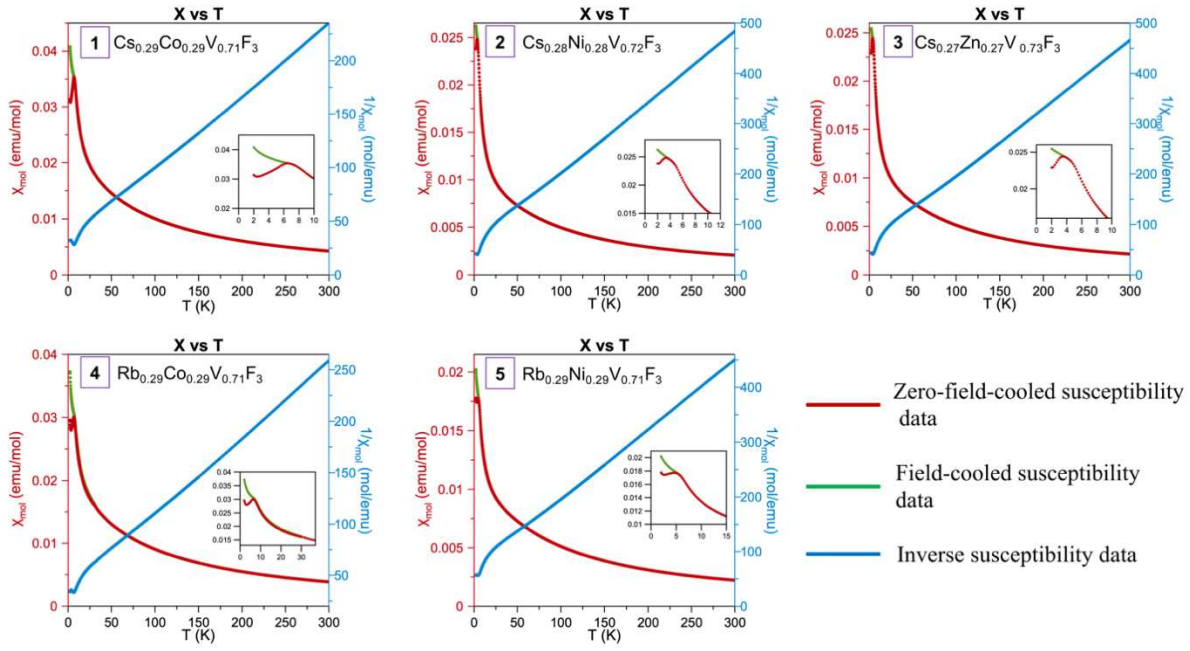

Figure 9. DC molar magnetic susceptibility (χ_{mol}) and inverse susceptibility ($1/\chi_{mol}$) vs. temperature plots for all HTB compounds. Magnetization vs. field plots for each material are provided in Figure S7 in the S.I.

The correlation between the size of the *A* cation and the Weiss temperature (θ_{CW}) has been studied in the past for A_xMO_3, where x = 0.33. It was determined that the absolute value of θ_{CW} decreases systematically as the size of the *A* cation increases.[40] This is because the distance between the magnetic cations becomes more significant as r_A increases, which reduces the strength

of the superexchange interaction between magnetic cations. As a result, A_xMO_3 exhibits a decrease in the θ_{CW} absolute value with increasing r_A. We also observed that the distances between magnetic ions in the Kagome layer of $Cs_{0.29}Co_{0.29}V_{0.71}F_3$ and $Cs_{0.28}Ni_{0.28}V_{0.72}F_3$ are considerably larger compared to $Rb_{0.28}Co_{0.28}V_{0.72}F_3$ and $Rb_{0.28}Ni_{0.28}V_{0.72}F_3$ (Figure 9). Presumably as a consequence of this, we observed a noticeable decrease in θ_{CW} for $Cs_{0.28}Ni_{0.28}V_{0.72}F_3$ (θ_{CW} = –41) compared to $Rb_{0.28}Ni_{0.28}V_{0.72}F_3$ (θ_{CW} = –52). However, the cobalt analogs do not exhibit significant differences in their Weiss temperatures. This might be due to a difference in the superexchange interactions between (Ni^{2+}–F–V^{3+}), (Ni^{2+}–F–Ni^{2+}), (Co^{2+}–F–V^{3+}), and (Co^{2+}–F–Co^{2+}).[41] Furthermore, we notice that the lengths of the A, B, and C sides of triangles in the Kagome layer are similar in both $Cs_{0.29}Co_{0.29}V_{0.71}F_3$ and $Cs_{0.28}Ni_{0.28}V_{0.72}F_3$. However, each side of the triangles (A, B, and C) in $Rb_{0.28}Co_{0.28}V_{0.72}F_3$ and $Rb_{0.28}Ni_{0.28}V_{0.72}F_3$ have significant differences (Figure 10). This observation suggests that the Rb ion inside the channel of the Kagome layer more extensively impacts the distortion of the Kagome layer compared to the Cs ion. A magnetic study of A_xVF_3 (A = Cs and Rb) has shown that the Weiss temperature of Rb_xVF_3 varies with the value of x, while the Weiss temperature of Cs_xVF_3 does not depend on the value of x.[16] This seems to support that the exchange interaction in the hexagonal bronze-type structures depends on the size of the *A* cation. Moreover, for the smaller cations, like Rb, exchange interactions also depend on the concentration of the *A* cation.

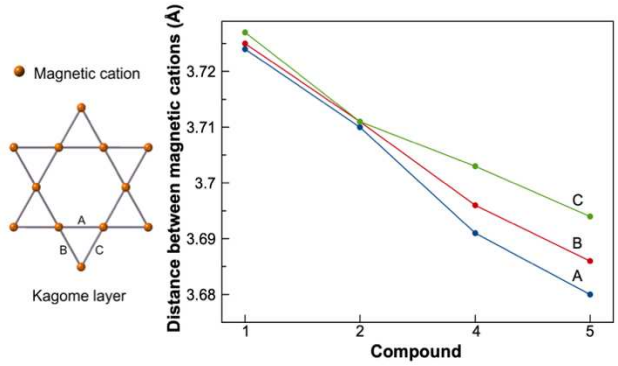

Figure 10. Representation of the length of A, B, and C sides in the Kagome layer of (1) $Cs_{0.29}Co_{0.29}V_{0.71}F_3$, (2) $Cs_{0.28}Ni_{0.28}V_{0.72}F_3$, (4) $Rb_{0.28}Co_{0.28}V_{0.72}F_3$, and (5) $Rb_{0.28}Ni_{0.28}V_{0.72}F_3$.

Conclusion:

A series of mixed-metal HTB fluorides with the formula $A_xM^{2+}_xM^{3+}_{(1-x)}F_3$ where x = 0.18−0.33 (*A* = Cs and Rb; M^{2+} = Co^{2+}, Ni^{2+} and Zn^{2+}, and M^{3+} = V^{3+}) were successfully synthesized using mild hydrothermal synthesis. $Cs_{0.29}Co_{0.29}V_{0.71}F_3$, $Cs_{0.28}Ni_{0.28}V_{0.72}F_3$, $Rb_{0.28}Co_{0.28}V_{0.72}F_3$, and $Rb_{0.28}Ni_{0.28}V_{0.72}F_3$ crystallize in the monoclinic space group $P2_1/m$, while $Cs_{0.27}Zn_{0.27}V_{0.73}F_3$ crystallizes in the $P2_1$ space group. The crystal structures of $Cs_{0.29}Co_{0.29}V_{0.71}F_3$, $Cs_{0.28}Ni_{0.28}V_{0.72}F_3$, and $Cs_{0.27}Zn_{0.27}V_{0.73}F_3$ were determined by SXRD. Structure solutions for $Rb_{0.28}Co_{0.28}V_{0.72}F_3$ and $Rb_{0.28}Ni_{0.28}V_{0.72}F_3$ were obtained by Rietveld refinement. Adjustments to the reaction conditions of the mild hydrothermal method resulted in a variety of different kinetically stable fluoride materials, including hydrated fluorides, β-pyrochlore fluorides and the HTB. These reaction outcomes highlight the sensitivity of the hydrothermal synthesis toward the solvent system, temperature, and quantity of starting reagent. This study achieved the synthesis of selected fluoride materials by tailoring the reaction conditions. Moreover, we observed the HTB to cubic β-pyrochlore structural phase transition at elevated temperatures, which indicates that the cubic β-pyrochlore structure is the high temperature stable phase. Magnetic measurements revealed that all five compounds exhibit a large negative Weiss temperature, indicating the presence of strong antiferromagnetic interactions in these materials. It is evident that the addition of M^{2+} ions (up to 30%) does not significantly alter the magnetic properties of Hexagonal Tungsten Bronze Fluorides when comparing the magnetic properties of all these compounds. The Kagome layers present in the HTB structure lead to the observed magnetic frustration of the materials. The large negative Weiss temperatures, along with magnetic transition temperatures below 6 K, yield frustration indexes between 7–13 for these compounds.

Acknowledgements

Financial support for this work was provided by the National Science Foundation under DMR-2221403 and is gratefully acknowledged.

Supporting Information

The Supporting Information is available free of charge at ???

Reaction condition data, elemental composition data, inductively coupled plasma optical emission spectroscopy (ICP-OES), crystal structure solution of $Cs_{0.28}Ni_{0.28}V_{0.72}F_3$, powder X-ray diffraction patterns, thermogravimetric and differential thermal analysis data, and magnetic plots.

Accession Codes

CCDC 2353016, 2353302, and 2353303 contain the supplementary crystallographic data for this paper. These data can be obtained free of charge via www.ccdc.cam.ac.uk/data_request/cif, or by emailing data_request@ccdc.cam.ac.uk, or by contacting The Cambridge Crystallographic Data Centre, 12 Union Road, Cambridge CB2 1EZ, UK; fax: +44 1223 336033.

References

1. Greedan, J. E. Geometrically Frustrated Magnetic Materials. *Funct. Oxide.* **2010**, *11*, 41-117.
2. Gardner, J. S.; Gingras, M. J. P.; Greedan, J. E. Magnetic Pyrochlore Oxides. *Rev. Mod. Phys.* **2010**, *82*, 53.
3. Greedan, J. E. Frustrated Rare Earth Magnetism: Spin Glasses, Spin Liquids and Spin Ices in Pyrochlore Oxides. *J. Alloys Compd.* **2006**, *408*, 444-455.
4. Reig-i-Plessis, D.; Hallas, A. M. Frustrated Magnetism in Fluoride and Chalcogenide Pyrochlore Lattice Materials. *Phys. Rev. Materials.* **2021**, *5*, 030301.
5. Biondo, V.; Sarvezuk, P. W. C.; Ivashita, F. F.; Silva, K. L.; Paesano, A.; Isnard, O. Geometric Magnetic Frustration in RE_2O_2S Oxysulfides (RE= Sm, Eu and Gd). *Mater. Res. Bull.* **2014**, *54*, 41-47.
6. Bordet, P.; Gelard, I.; Marty, K.; Ibanez, A.; Robert, J.; Simonet, V.; Canals, B.; Ballou, R.; Lejay, P. Magnetic Frustration on a Kagomé Lattice in $R_3Ga_5SiO_{14}$ Langasites with R= Nd, Pr. *J. Phys.: Condens. Matter.* **2006**, *18*, 5147.
7. Krizan, J. W.; Cava, R. J. $NaCaCo_2F_7$: A Single-Crystal High-Temperature Pyrochlore Antiferromagnet. *Phys. Rev. B.* **2014**, *89*, *214401*.
8. Krizan, J. W.; Cava, R. J. $NaCaNi_2F_7$: A Frustrated High-Temperature Pyrochlore Antiferromagnet with S=1Ni^{2+}. *Phys. Rev. B.* **2015**, *92*, 014406.
9. Morrison, G.; Masachchi, L. W.; Tisdale, H. B.; Chang, T.; Jones, V. G.; Zamorano, K. P.; Breton, L. S.; Smith, M. D.; Chen, Y.-S.; zur Loye, H.-C. Polymorphism in A_3MF_6 (A= Rb, Cs; M= Al, Ga) Grown using Mixed Halide Fluxes. *Dalton Trans.* **2023**, *52*, 8425-8433.
10. Molokeev, M. S.; Bogdanov, E. V.; Misyul, S. V.; Tressaud, A.; Flerov, I. N. Crystal Structure and Phase Transition Mechanisms in $CsFe_2F_6$. *J. Solid State Chem.* **2013**, *200*, 157-164.
11. Ferey, G. In *Mixed Valence Iron and Chromium Fluorides. Bronzes and Related Compounds. Chemistry, Structure and Magnetism*; 1991; pp 155-174.
12. Yeh, Y. K.; Hong, Y. S.; Boo, W. O. J.; Mattern, D. L. High-temperature DTA Studies of A_xMF_3 compounds (A= K, Rb, Cs; M= V, Cr; and x= 0–1.0). *J. Solid State Chem.* **2005**, *178*, 2991-2196.
13. Boo, W. O. J.; Williamson, R. F.; Baker, K. N.; Hong, Y. S. Lower Valence Fluorides of Vanadium, Chromium, and Iron A_XMF_3 (A = K, Rb, or Cs: M = V. Cr, or Fe; and x=0 to 1). *Mol. Cryst. Liq. Cryst.* **1984**, *107*, 195-210.
14. Hong, Y. S.; Williamson, R. F.; Boo, W. O. J. Lower Valence Fluorides of Vanadium. 3. Structures of the Pseudohexagonal A_xVF_3 Phases (where A= potassium, rubidium, thallium, or cesium). *Inorg. Chem.* **1979**, *18*, 2123-2125.
15. Hong, Y. S.; Williamson, R. F.; Boo, W. O. J. Lower Valence Fluorides of Vanadium. 5. Dependence of Structure and Magnetic Properties of Tetragonal K_xVF_3 on Composition. *Inorg. Chem.* **1980**, *19*, 2229-2233.
16. Hong, Y. S.; Williamson, R. F.; Boo, W. O. J. Lower Valence Fluorides of Vanadium. 6. Dependence of Structure and Magnetic Properties of the Pseudohexagonal A_xVF_3 Compounds on Composition. *Inorg. Chem.* **1981**, *20*, 403-409.
17. Hong, Y. S.; Williamson, R. F.; Boo, W. O. J. Lower Valence Fluorides of Vanadium. 7. Dependence of Structure and Magnetic Properties of the Modified Pyrochlores Rubidium

Vanadium Fluoride (Rb_xVF_3) and Cesium Vanadium Fluoride (Cs_xVF_3) on Composition. *Inorg. Chem.* **1982**, *21*, 3898-3903.
18. Grey, I. E. Kagomé Networks of Octahedrally Coordinated Metal Atoms in Minerals: Relating Different Mineral Structures Through Octahedral Tilting. *Mineral. Mag.* **2020**, *84*, 640-552.
19. Reis, K. P.; Ramanan, A.; Whittingham, M. S. Synthesis of Novel Compounds with the Pyrochlore and Hexagonal Tungsten Bronze Structures. *J. Solid State Chem.* **1992**, *96*, 31-47.
20. Berseneva, A. A.; zur Loye, H.-C. Advances in Chalcogenide Crystal Growth: Flux and Solution Syntheses, and Approaches for Postsynthetic Modifications. *Cryst. Growth Des.* **2023**, *23*, 5368-5383.
21. Klepov, V. V.; Pace, K. A.; Berseneva, A. A.; Felder, J. B.; Calder, S.; Morrison, G.; Zhang, Q.; Kirkham, M. J.; Parker, D. S.; zur Loye, H.-C. Chloride Reduction of Mn^{3+} in Mild Hydrothermal Synthesis of a Charge Ordered Defect Pyrochlore, $CsMn^{2+}Mn^{3+}F_6$, a Canted Antiferromagnet with a Hard Ferromagnetic Component. *J. Am. Chem. Soc.* **2021**, *143*, 11554-11567.
22. Keerthisinghe, N.; Ayer, G. B.; Smith, M. D.; zur Loye, H.-C. Comparative Study on Crystal Structures and Synthetic Techniques of Ternary Hafnium/Zirconium Fluorides. *Inor. chem.* **2023**, *62*, 12089-12098.
23. Keerthisinghe, N.; Klepov, V. V.; Zhang, E.; Smith, M. D.; Egodawatte, S.; Foulger, S. H.; zur Loye, H.-C. Hydrothermal synthesis and properties of $M^{II}M^{III}F_5(H_2O)_7$ ($M^{II} = Co^{2+}$ and Ni^{2+}, $M^{III} = Mn^{3+}$, Ga^{3+}, and In^{3+}). *Solid State Sci.* **2020**, *108*, 106374.
24. Rabenau, A. The Role of Hydrothermal Synthesis in Preparative Chemistry. *Angewandte Chemie.* **1985**, *24*, *1026-1040*.
25. Demazeau, G.; Largeteau, A. Hydrothermal/Solvothermal Crystal Growth: an Old but Adaptable Process. *Z. Anorg. Allg. Chem.* **2015**, *641*, 159-163.
26. Demazeau, G. Solvothermal Processes: New Trends in Materials Chemistry. *J. Phys.: Conf. Ser.* **2008**, *121*, 082003.
27. Songvilay, M.; Rodriguez, E. E.; Lindsay, R.; Green, M. A.; Walker, H. C.; Rodriguez-Rivera, J. A.; Stock, C. Anharmonic Magnon Excitations in Noncollinear and Charge-Ordered $RbFe^{2+}Fe^{3+}F_6$. *Phys. Rev. Lett.* **2018**, *121*, *087201*.
28. APEX3 Version 2019.1-0 and SAINT+ Version 8.40A. **2019**,
29. Krause, L.; Herbst-Irmer, R.; Sheldrick, G. M.; Stalke, D. Comparison of Silver and Molybdenum Microfocus X-ray Sources for Single-Crystal Structure Determination. *J. Appl. Crystallogr.* **2015**, *48*, 3-10.
30. Sheldrick, G. M. SHELXT– Integrated Space-Group and Crystal-Structure Determination. *Acta Cryst. A.* **2015**, *71*, 3-8.
31. Hübschle, C. B.; Sheldrick, G. M.; Dittrich, B. ShelXle: a Qt graphical user interface for SHELXL. *J. Appl. Crystallogr.* **2011**, *44*, *1281-1284*.
32. Spek, A. L. Structure Validation in Chemical Crystallography. *Acta Crystallogr D Biol Crystallogr.* **2009**, *65*, 148-155.
33. Dinnebier, R. E.; Leineweber, A.; Evans, J. S. O. *Rietveld refinement: practical powder diffraction pattern analysis using TOPAS*; Walter de Gruyter GmbH & Co KG: Berlin, Boston, 2018.

34. Morrison, G.; zur Loye, H.-C. Simple Correction for the Sample Shape and Radial Offset effects on SQUID Magnetometers: Magnetic Measurements on Ln_2O_3 (Ln=Gd, Dy, Er) Standards. *J. Solid State Chem.* **2015**, *221*, 334-337.
35. Ayer, G. B.; Klepov, V. V.; Pace, K. A.; zur Loye, H.-C. Quaternary Cerium(IV) Containing Fluorides Exhibiting Ce_3F_{16} Sheets and Ce_6F_{30} Frameworks. *Dalton Trans.* **2020**, *49*, 5898-5905.
36. Ayer, G. B.; Klepov, V. V.; Smith, M. D.; zur Loye, H.-C. Mild Hydrothermal Synthesis of the Complex Hafnium-Containing Fluorides $Cs_2[M(H_2O)_6][Hf_2F_{12}]$ (M = Ni, Co, Zn), $CuHfF_6(H_2O)_4$, and $Cs_2Hf_3Mn_3F_{20}$ Based on HfF_7 and HfF_6 Coordination Polyhedra. *Inorg. Chem.* **2019**, *58*, 13049-13057.
37. Keerthisinghe, N.; Berseneva, A. A.; Klepov, V. V.; Morrison, G.; zur Loye, H.-C. A Geometrically Frustrated Family of $M^{II}M^{III}F_5(H_2O)_2$ Mixed–Metal Fluorides with Complex Magnetic Interactions. *Inorg. Chem.* **2021**, *60*, 14318-14329.
38. Masachchi, L. W.; Keerthisinghe, N.; Morrison, G.; Berseneva, A. A.; Smith, M. D.; zur Loye, H.-C. Crystal Growth and Magnetism of Transition Metal Pyrochlore Fluorides. *Inor. chem.* **2023**, *62*, 13793-13801.
39. Mugiraneza, S.; Hallas, A. M. Tutorial: a Beginner's Guide to Interpreting Magnetic Susceptibility Data with the Curie-Weiss Law. *Commun. Phys.* **2022**, *5*, 95.
40. Ivanov, S. A.; Sahu, J. R.; Voronkova, V. I.; Mathieu, R.; Nordblad, P. Structure and Magnetism in Hexagonal Tungsten Bronze Metal Oxides $AM_{1/3}W_{8/3}O_9$ (A–K, Rb, Cs; M–Cr, Fe). *Solid State Sci.* **2015**, *40*, 44-49.
41. Banks, E.; Deluca, J. A.; Berkooz, O. Preparation, Magnetic Properties and Mossbauer Study of the Modified Pyrochlores $M^{II}M^{III}F_6A$. *J. Solid State Chem.* **1973**, *6*, 569-573.

For Table of Contents Use Only

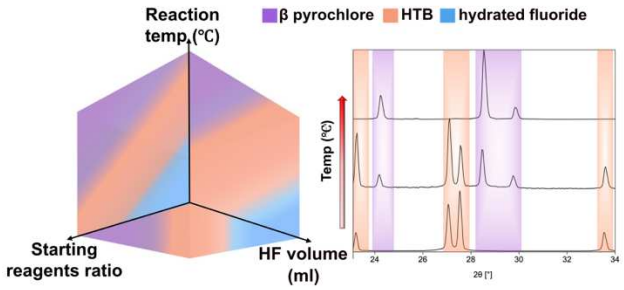

Synopsis

The synthesis, crystal structure, and magnetic properties of new mixed-metal hexagonal tungsten bronze fluorides are described. In addition, the sensitivity of the mild hydrothermal synthesis with respect to its reaction temperature, hydrofluoric acid volume, and starting reagents is discussed.